Investigation of Non-uniform Waterjet Pump Inflow for a Range of Ship Speeds

Phillip Duerr and Karl von Ellenrieder
Department of Ocean & Mechanical Engineering
Florida Atlantic University
Dania Beach, FL 33004 USA
pduerr@fau.edu, ellenrie@fau.edu

***Abstract*—Numerical simulations are used to generate a velocity field entering the pump of a waterjet propelled ship so that the level of non-uniformity in axial velocity can be evaluated. Non-uniform axial velocity entering the pump causes unsteady loading of the rotor blades resulting in noise, vibrations, and can increase the risk of rotor cavitation. The hull form modeled in this study is the *R.V. Athena*, fitted with a waterjet propulsion system. The ship speeds in this investigation correspond to Froude numbers between 0.34 and 0.84 and Reynolds numbers between 3.6 x 10^8 and 9.0 x 10^8. The pump shaft speed and flow rate are determined via calm water resistance data from experiments and the pump curves for the axial flow pump modeled. The numerical simulations are steady single phase and do not include the free surface. In all of the numerical simulations the hull geometry is kept at a fixed draft and on even keel. The variation in axial velocity is quantified by total distortion coefficient, harmonic components, and rotor section inflow angles. Using harmonic analysis, it is shown that the non-dimensional wake entering the pump exhibits a mean axial velocity component that varies proportionally to nozzle velocity ratio and harmonics of constant amplitude and phase, for all ship speeds. Thus, the wake pattern at any ship speed can be approximated using the harmonic content of the wake at one ship speed, and scaling the mean axial velocity. It is also found that this hull and pump configuration resulted in the pump operating at a fixed pump flow coefficient for all ship speeds investigated. The result is that the average rotor section inflow angles are also constant over the speed range. This is ideal for a rotor with a fixed pitch distribution because the mean angle of attack on a given rotor section will be independent of ship speed.**

Keywords—Waterjet inlet; flow distortion; ship propulsion

I. INTRODUCTION

Waterjets are an increasingly common means of propulsion for high speed craft. One aspect of particular concern is the non-uniform velocity distribution entering the pump of the waterjet. Impeller inflow is an important consideration because the inflow determines blade loading, vibrations, and cavitation. Brandner and Walker [3] investigated the influence of pump wake fraction, $(1-w)_3$, and the thickness of the ingested boundary layer on ramp separation, lip cavitation, and the velocity distribution entering the pump. However, the measurements of non-uniform axial velocity entering the pump were only carried out at one Reynolds number. Bulten [4] expanded the quantification of pump inflow non-uniformity by defining a total distortion coefficient, using Fourier analysis as a metric of variations in axial velocity at a given radius, and reported the variations in angle of attack that a rotor section would see at a given radius based on the pump shaft speed. The spectrum representing the variations in axial velocity entering the pump are not reported, and variations in rotor section inflow angle are only reported at one value of pump wake fraction.

This paper explores the non-uniform velocity distribution entering the pump of the waterjet for the *R.V. Athena* over a range of steady ship speeds. In this study, hull boundary layer thickness, required thrust, and pump operating point are accounted for at each ship speed. Non-uniformity is reported in terms of total wake distortion coefficient and the spectrum of axial velocity at a typical radius. The velocity distribution entering the pump is simulated for the full scale ship using Computational Fluid Dynamics (CFD). Simulations cover the Froude number range$0.34 \leq Fn \leq 0.84$, which corresponds to ship speeds of $14 \leq V_0 \leq 35$ kts. With Froude number defined as,

$$Fn \equiv V_0 \Big/ \sqrt{g L_{WL}} \tag{1}$$

where L_{WL} and g are the length along the waterline and the acceleration due to gravity, respectively.

The *R.V. Athena*, seen in Fig. 1, is a high speed round bilge hull form. The ship is modeled with the twin waterjet propulsion system described in Allison et al. [2]. The principle characteristics of the *R.V. Athena* are listed in Table I.

Where possible, the ITTC terminology and definitions are employed [10]. Stations refer to the ITTC stations displayed in Fig. 2. Properties such as area, A_i, and average velocity V_i, are given the subscript i to denote the station. Doubled subscripts, ij, indicate a property existing between stations i and j.

II. SHIP OPERATING POINT

Full scale calm water total resistance R_T, is predicted via the ITTC 1957 method [7] and from the model scale resistance experiments conducted by Crook [6]. The resistance

Phillip Duerr is supported by a SMART Ph.D. Fellowship Program. This work was supported, in part, by the U.S. Office of Naval Resarch T-Craft Tools Program administered by Ms. K Cooper.

coefficients are shown in Fig. 3. Powering coefficients for the wake fraction at Station 1a, $(1\text{-}w)_{1a}$, and thrust deduction, $(1\text{-}t)$, are assumed to be 0.9 and 1.0, respectively, for all ship speeds [2].

Fig. 1. The *R.V. Athena* at sea [10].

TABLE I SHIP AND PROPULSOR PRINCIPLE CHARACTERISTICS

Ship			
Length along waterline	L_{WL}	46.94	m
Maximum Beam	B_{Max}	6.87	m
Draft	T_0	1.70	m
Still wetted surface area	S_0	316	m^2
Waterjet System			
Rotor Diameter	D_3	1.06	m
Nozzle Diameter	D_6	0.72	m

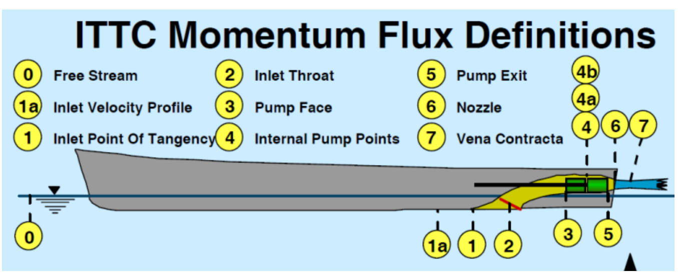

Fig. 2. ITTC waterjet stations [10].

The required thrust T, is calculated using the relationship for thrust deduction, $(1\text{-}t)$,

$$T = (1-t)\, R_T \,. \tag{2}$$

Assuming no trim or nozzle deflection, and ignoring the influence of the vena contracta, the thrust developed by accelerating the flow through the waterjet is,

$$T \equiv \rho V_6 A_6 \left(V_6 - (1-w)_{1a} V_0\right), \tag{3}$$

where ρ is the fluid density. Nozzle velocity ratio (NVR),

$$NVR \equiv V_6 / V_0 \,, \tag{4}$$

where V_i is the average velocity at station i in Fig. 2, is sufficient to define the flow rate through the system.

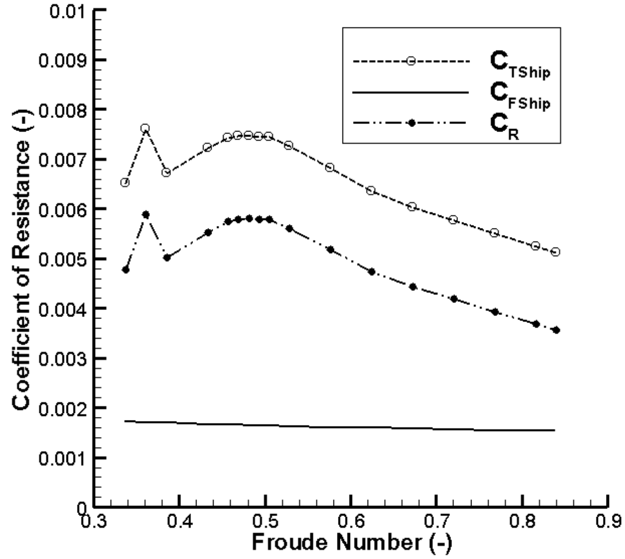

Fig. 3. Calm water unappended resistance coefficients [6].

By introducing the waterjet thrust loading coefficient (C_{TWJ}),

$$C_{TWJ} \equiv \frac{T}{\frac{1}{2}\rho V_0^{\,2} A_6}\,, \tag{5}$$

and solving (3) in terms of nozzle velocity ratio under the condition that NVR>0 results in,

$$NVR = \frac{1}{2}\left((1-w)_{1a} + \sqrt{(1-w)_{1a}^{\;2} + 2C_{TWJ}}\right). \tag{6}$$

The head rise across the pump, H_{35}, that is required to achieve the desired nozzle velocity ratio is estimated using the method presented by Allison [1],

$$H_{35} = \frac{1}{2g}\left(\frac{V_6^{\,2}}{\eta_{56}} - V_{1a}^{\;2}\eta_{13}\right) + z_{ShaftCL}\,, \tag{7}$$

where η_{13}, η_{56}, and $z_{ShaftCL}$ are the inlet efficiency, nozzle efficiency, and height of the shaft centerline above the static waterline, respectively. Nominal values of the inlet and nozzle efficiencies are taken to be 0.83 and 0.99 Allison [1]. The pump shaft speed is determined using the model scale pump curves for the *R.V. Athena* waterjet pump presented in [11] and the non-dimensional pump parameter, $(K_H/K_{QJ}^{\,2})$,

$$\left(\frac{K_H}{K_{Q_J}^{\;2}}\right) \equiv \frac{gH_{35}D_3^{\,4}}{Q_J^{\,2}}\,, \tag{8}$$

whereD_3 and Q_J are pump diameter and jet volumetric flow rate respectively. At steady state, the pump will operate where the required head rise to propel the ship, from the pump parameter $(K_H/K_{QJ}^{\,2})$, matches the head rise available from the waterjet pump. Shaft speed, n, is then computed from the pump flow coefficient, K_{QJ},

$$K_{Q_J} \equiv \frac{Q_J}{nD_3^{\,3}} . \quad (9)$$

With all of the parameters determined for a given ship speed, a CFD simulation is run to compute the flow field around the hull and through the waterjet inlet. Velocities at Station 3 are extracted from the flow field to be analyzed further.

III. Analysis of Inflow

A means of quantifying the level of non-uniformity in a wake is through the total distortion coefficient, ζ,

$$\zeta \equiv \frac{1}{Q_J} \int_{A_3} \sqrt{\left(V_n - V_3\right)^2}\, dA , \quad (10)$$

where V_n is the component of velocity normal to the surface of integration.. The circumferential variations in axial velocities, can be approximated by a finite Fourier series,

$$\frac{V_x}{V_0}(\theta) \approx \sum_{n=0}^{N} d_n \cos(n\theta + \phi_n) , \quad (11)$$

where θ, d_n, and φ_n are the circumferential position, nth harmonic amplitude and phase respectively. Neglecting the circumferential component of velocity, the rotor section inflow angle, β, is defined as,

$$\beta \equiv \arctan\left(\frac{V_x}{\omega_{Shaft} r}\right), \quad (12)$$

where ω_{Shaft}, and r are angular shaft speed and rotor section radius. Deviations from the mean inflow angle, $\Delta\beta_{r/R}$, at a given radius, are given by,

$$\Delta\beta_{r/R} = \beta_{r/R} - \overline{\beta_{r/R}} , \quad (13)$$

where $\overline{\beta_{r/R}}$, is the circumferential mean inflow angle. Assuming that shaft speed is constant and that the rotor is not cavitating, unsteady loading arises due to variations in inflow angle.

Another means of assessing performance is rotor advance coefficient, J_A, which is defined as,

$$J_A \equiv \frac{V_3}{nD_3} , \quad (14)$$

and describes how the rotor is operating in an aggregate sense. Rotor section inflow angles are chosen over rotor advance coefficient as they allow for investigation of inflow variations circumferentially and in the spanwise direction.

IV. CFD Simulations

The flow around the hull and through the waterjet inlet is computed using the commercially available ANSYS Fluent v13 software package. The steady incompressible 3D-RANS equations are simulated using the Spalart-Allmaras turbulence model [8]. Wall functions are used to resolve the boundary layer near viscous walls. A finite volume approach [9] is used to solve the transport equations on an unstructured mesh. The flow field is assumed to be single phase.

The computational domain employs centerline symmetry, a boundary at the static free surface, outboard of the hull, and below the hull. Only flow along the aft portion of the hull and through the waterjet system is within the computational domain. The computational domain can be seen in Fig. 4. Normalized dimensions of the computational domain are listed in Table II, where upstream/downstream are relative to the extents of the waterjet inlet fairing. The geometry of the hull, waterjet, and bounds of the computational domain are held fixed for all simulations.

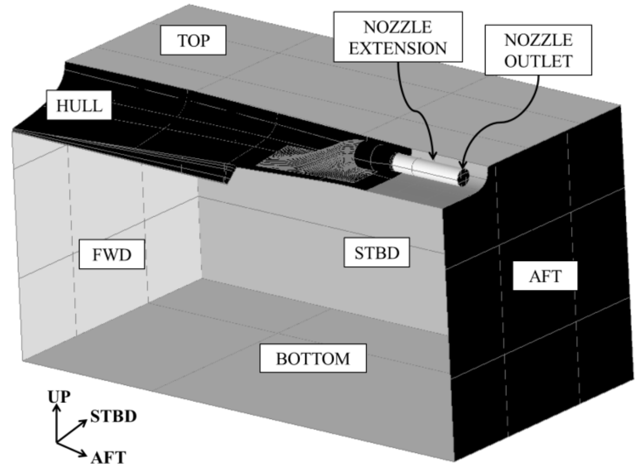

Fig. 4. Computational domain used for all CFD simulations.

Table II Ship and Propulsor Principle Characteristics

Direction	Distance
$L_{Upstream}/D_3$	11.3
$L_{Downstream}/D_3$	4.5
$L_{Nozzle\ Extension}/D_6$	5.0
$(B_{Domain}/2)/(B_{Max}/2)$	3.0
$Depth_{Domain}/T_0$	6.4

The computational mesh is an unstructured hexahedral mesh and is created using ANSYS ICEMCFD v13.0 software. Despite being exported as an unstructured mesh, the computational domain is discretized using a multi-block approach and then converted to a single unstructured domain.

Since wall functions are employed the height of the first cell off of viscous wall boundaries, y_1, is set to a nominal distance from the wall of 30 wall units. The first cell height is determined via the relation,

$$\frac{y_1}{L_{WL}} = \frac{y^+}{Rn\left(C_f/2\right)^{1/2}} , \quad (15)$$

where y^+, Rn, and Cf are the non-dimensional wall coordinate, Reynolds number using waterline length, and friction coefficient from the ITTC 1957 friction line, respectively. The cell heights expand in the direction normal to viscous wall boundaries as a geometric series with an expansion ratio of 1.2. The entire computational domain is comprised of approximately 4×10^5 cells.

The boundary conditions used in all of the simulations presented are summarized in Table III. Centerline symmetry is exploited to reduce the size of the computational domain. Velocities at the inlet plane are set using a $1/7^{th}$ power law turbulent boundary layer velocity profile normal to the hull. Downstream, the outlet boundary is set to a constant pressure outlet condition. The surfaces of the hull, centerline-keel, inlet duct, pump casing, stator hub, and nozzle are all modeled as viscous walls. A zero shear stress wall is applied at the mean still free surface. The flow behind the transom is not included in the computational domain. Additionally, the rotor and stator blades are not modeled in the simulations. Mass flow rate through the waterjet system is set by lowering pressure on the outlet of the waterjet system. The waterjet system pressure outlet is not applied at the exit to the nozzle, but at the end of a cylinder that extends about five nozzle diameters downstream. The walls of the cylinder are set to zero shear stress walls. Although this method does achieve the required flow rate through the waterjet system, it does not account for the energy added to the flow in the pump stage. The pump shaft and rotor hub surfaces are set to viscous walls with tangential velocity from shaft speed.

TABLE III BOUNDARY CONDTIONS

Boundary Type	**Surfaces**
Velocity Inlet	Forward Plane
Zero Shear Wall	Top, Outboard, Bottom, Nozzle Extension
Symmetry	Centerline Plane
Pressure Outlet	Aft Plane, Nozzle Outlet
Wall	Hull, Waterjet Casing, Stator Hub
Moving Wall	Pump Shaft, Pump Rotor Hub

The following criteria are used to determine whether a simulation has converged: 1) the target mass flow rate through the water jet system is matched; 2) the residuals of continuity and momentum have dropped more than four orders of magnitude; and 3) additional iterations produce no visible change in the wake pattern at Station 3. The flow field from each simulation is also visually inspected for non-physical flow features and mesh dependence.

V. MODEL SCALE VALIDATION

The velocity profile at Station 3 is available for the *R.V. Athena* during model scale powering experiments for a Froude number of 0.6 [5]. Simulations at model scale are run to determine the most applicable turbulence model, boundary conditions, and the amount of mesh resolution required to resolve important flow features. The wake at Station 3 from experiments and the CFD simulation are presented in Fig. 5 and Fig. 6, respectively. The region in figure Fig. 5 that is below and to the right of the shaft is left blank because during the experiment the line of sight of both Laser Doppler Velocimetry (LDV) probes was blocked by the shaft.

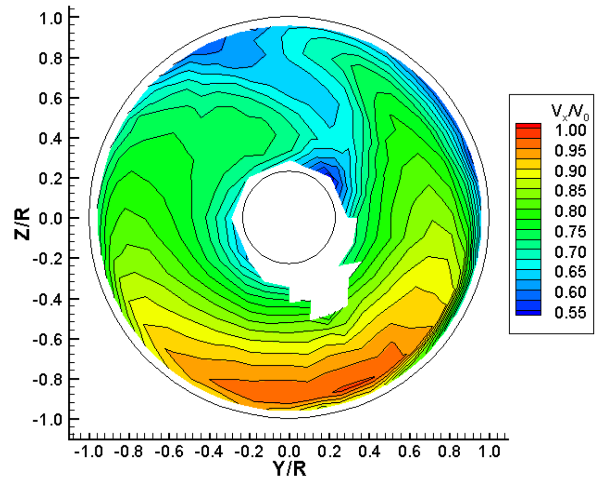

Fig. 5. Model experiment LDV wake survey [1], contours of non-dimensional axial velocities at Station 3.

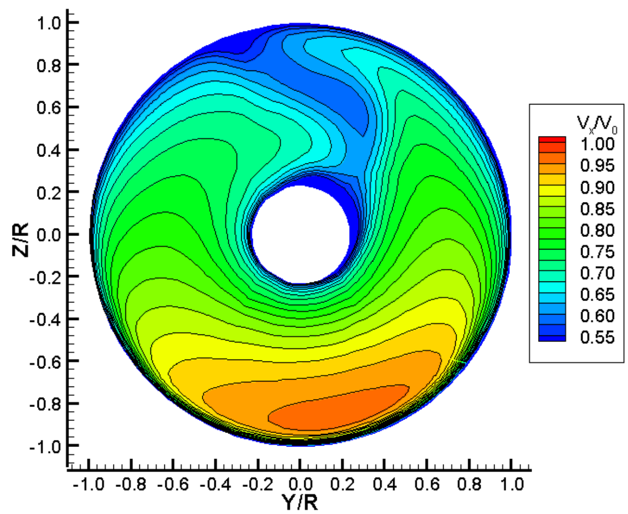

Fig. 6. CFD computation at model scale, contours of non-dimensional axial velocities at Station 3.

The primary features of the wake at Station 3 are: 1) the velocity deficit due the shaft extending from the center of the disk to top dead center (TDC); 2) the shape and location of the region of high velocity flow near bottom dead center (BDC); 3) the region of lower velocity flow in the upper portion of the disk. The wakes from the experiment and simulation both capture the three previously mentioned features of the wake, and between the two methods, the important features of the wake are very similar in shape and location. The main difference between the experimental results and the simulation are the magnitude of axial velocity. The differences in axial velocity are slight, but most noticeable in the wake deficit due to the shaft where the simulation reported lower axial velocity than the experimental wake survey, and in the region of high speed flow, the simulation did not capture the same maximum axial velocity as the experiment.

VI. RESULTS

Typical non-dimensionalized axial velocity contours at Station 3 are shown in Fig. 7 to Fig. 9, for a Froude numbers of 0.384, 0.6, and 0.815. Flow features seen the wakes are typical of the wake at station 3 for the entire range of Froude numbers investigated. At each ship speed the wake at Station 3 exhibits a shaft velocity deficit that is curled, a region of highest velocity flow near BDC and slightly outboard and a lower velocity flow in the top portion of the disk. Despite these similarities, the magnitudes of the axial velocities at Station 3 do change as ship speed changes.

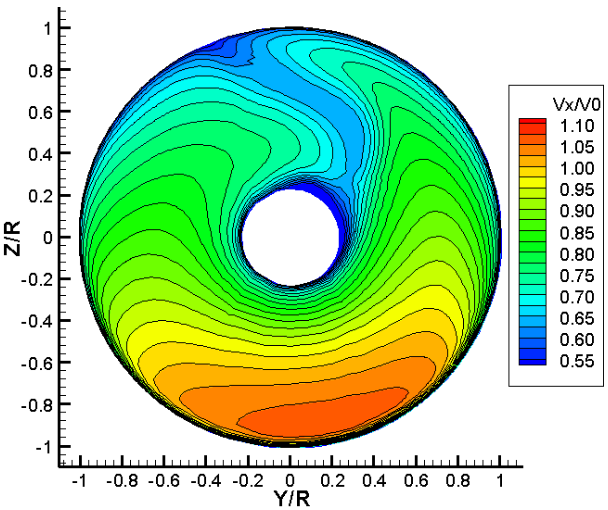

Fig. 7. Contours of non-dimensional axial velocity at Station 3 (*Fn*=0.384).

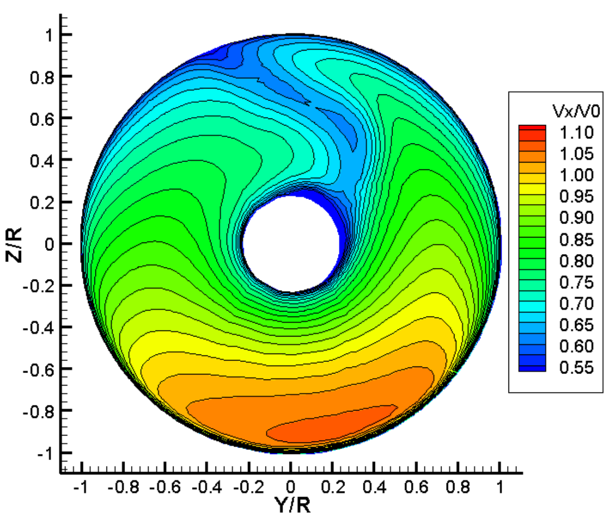

Fig. 8. Contours of non-dimensional axial velocity at Station 3 (*Fn*=0.6).

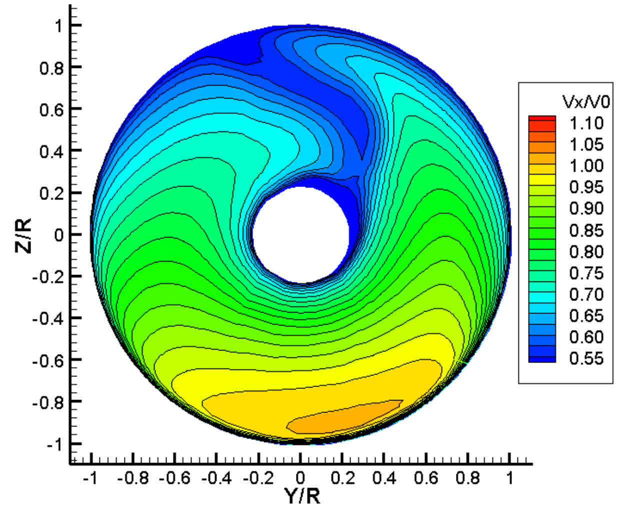

Fig. 9. Contours of non-dimensional axial velocity at Station 3 (*Fn*=0.815).

The range of total wake distortion and wake fraction at Station 3 are, presented in Fig. 10. The values for wake distortion shown in Fig. 10 are comparable to the results presented by Bulten [4], which reports a value of wake distortion of 0.15 for a wake fraction at Station 3 of 0.77 and a value of wake distortion of 0.12 for a wake fraction at Station 3 of 0.91.Since the wake fraction at Station 3 is an average velocity ratio it describes the amount of acceleration/diffusion from free stream to the pump face. Diffusion tends to increase flow non-uniformity, as is illustrated in Fig. 10 where total distortion and wake fraction are negatively correlated.

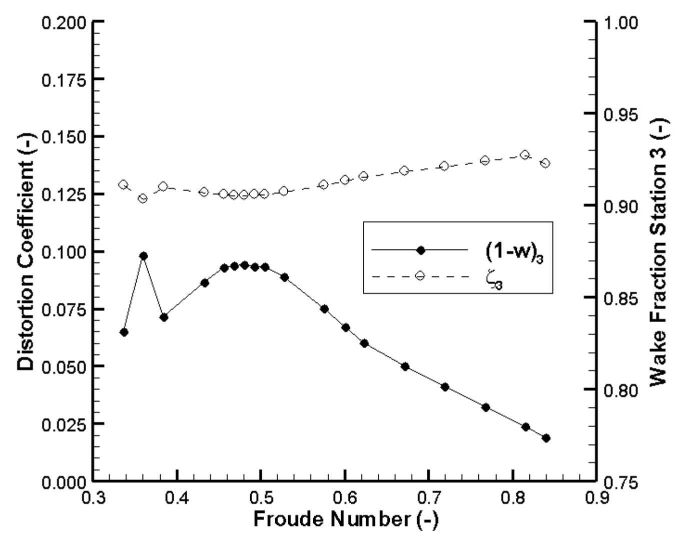

Fig. 10. Wake fraction and wake distortion at Station 3.

The amplitude and phase of the non-dimensional axial velocity are shown in Fig. 11 and Fig. 12, for a non-dimensional radius of 0.65. Only the mean and first three harmonics of the amplitude spectrum are shown, because the amplitude of higher harmonics diminishes rapidly. The harmonic amplitudes and phase in Fig. 12 are typical of non-dimensional radii in the range $0.25 \leq r/R \leq 0.95$.

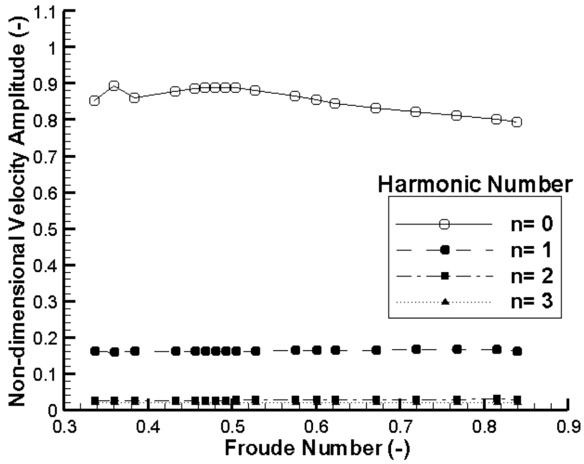

Fig. 11. Amplitude spectrum of non-dimensional axial velocity at a non-dimensional radius of 0.65.

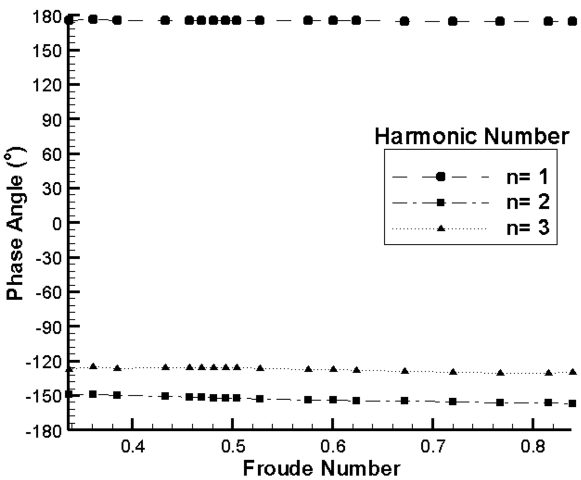

Fig. 12. Phase spectrum of non-dimensional axial velocity at a non-dimensional radius of 0.65.

When inspecting the wake contours at Station 3 over the range of Froude numbers it appears that the location of the velocity deficit from the shaft and the location of the maximum axial velocity do not vary substantially over the range of Froude numbers. This assertion is reinforced by the fact that there is almost no variation in amplitude or phase of the harmonic content of the wake, only changes in the mean component of the wake.

Since the mean component of axial velocity is the only portion of the spectrum that contributes to the net mass flux, it is appropriate to scale the mean component of velocity by the waterjet pump flow rate. This allows a wake profile at one ship speed to be used to approximate the wake profile at another ship speed. The approximate wake profile can be generated by scaling only the magnitude of the mean component of the axial velocity by the relative change in flow rate between the two ship speeds. The phase and non-dimensional amplitude of the harmonics can simply be superimposed without any scaling.

Despite the changes in the mean velocity displayed over the range of ship speeds, the mean inflow angles (Fig. 13) at a given radius varied by less than 1^{o} over the entire range of ship speeds investigated. This is due to two factors, the magnitude of the mean flow scales with the relative change nozzle velocity ratio, and the pump flow coefficient is approximately constant. For the ship and pump used in this analysis, the pump flow coefficient varied by -0.2% to 1.3% of the value for pump flow coefficient at the ship design speed (Froude number of 0.6). Since the pump flow coefficient is approximately constant, both the mean axial flow at a given radius and shaft RPM change by the same proportion as the change in nozzle velocity ratio.

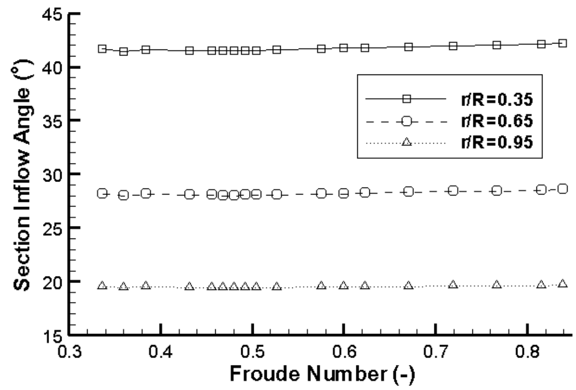

Fig. 13. Mean inflow angle at several radii.

Since rotor section average inflow angles are independent of ship speed, the sections of a fixed pitch rotor will continue to operate at design angle of attack for any steady ship speed. The only significant angle of attack loading will be due to the circumferential variations in axial velocity.

The minimum and maximum deviations from mean inflow angle are also nearly constant and only vary by one to two degrees over the entire range of ship speeds, Fig. 14.

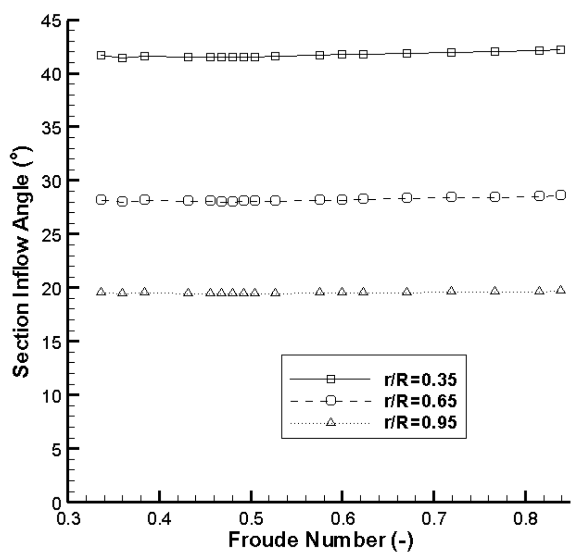

Fig. 14. Maximum and minimum deviations from mean inflow angle in one revolution at several radii.

The variation in rotor inflow angle is significant because as a foil section operates at angle of attacks further from the ideal angle of attack, a region of very low pressures near the leading edge forms. This region is referred to as a leading edge suction peak. The pressure in the suction peak tends to be the minimum pressure for a given foil section, and therefore this region of the foil section will begin to cavitate first.

VII. CONCLUSIONS

In this work the flow through a waterjet inlet is simulated for a full scale ship over a range of ship speeds. The propulsion point for each ship speed simulated is determined using resistance data from towing tank experiments and pump curves derived from experiments. Powering coefficients, inlet efficiency, and nozzle efficiency for the full scale ship are assumed to be constant for all ship speeds, and typical values are used to determine the operating point for the waterjet pump. The ship was held at fixed sinkage and trim for all ship speeds. Additionally, the CFD simulations only considered the flow to be single phase, and therefore neither the free surface nor cavitation is modeled.

The analysis of the pump inflow consisted of an aggregate distortion metric, harmonics of axial velocity at a given radii, and relative rotor section inflow angles. Results of the study support the following findings:

- As with other diffusers, increasing the amount of diffusion of the flow upstream of the pump results in higher levels of flow non-uniformity at the pump face.
- The non-dimensional mean flow component of the wake changes over the speed range, and is proportional to the relative change in nozzle velocity ratio. The non-dimensional axial flow harmonics and phase angle are independent of ship speed.
- Pump inflow at a new ship speed can be approximated by scaling the magnitude of the mean flow component of the wake by the relative change in pump flow rate (i.e. the relative change in nozzle velocity ratio) and superimposing the alternating components of the wake.
- The average rotor section inflow angle remains constant over the ships speed range, because the pump flow coefficient, K_{QJ}, remains constant.

Having both pump flow coefficient and the harmonic content of the wake independent of steady ship speed are very favorable properties of a waterjet system. The combination of these two properties results in rotor section angle of attack variations which are independent of steady ship speed. However, ships do not always operate ahead, at steady ship speeds, and at a fixed hull attitude. Other ship operating conditions should be investigated in order to evaluate the properties of the inflow to the pump.

ACKNOWLEDGMENTS

The authors would like to thank several employees at the Naval Surface Warfare Center–Carderock Division for their contributions to this project: Dr. Chris Chesnakas for his experimental work with Model 5600, Seth Schroeder for his guidance on meshing and RANS simulations, and Dr. Scott Black, for his guidance.

REFERENCES

[1] J. Allison, "Marine Waterjet Propulsion," *SNAME Transactions, Vol. 101,* pp. 275-335, 1993.

[2] J. Allison, A. Becnel, J. Purnell, J. Gorski, J. Hoyt III and M. Wilson, "Research in waterjet inlet, hull, and jet interactions," in *International Conferenceon Waterjet Propulsion III*, Gothenburg, Sweden, 2001.

[3] P. A. Brandner and G. J. Walker, "An Experimental Investigation Into the Performance of a Flush Water-Jet Inlet," *Journal of Ship Research, Vol. 51, No. 1,* p. 1–21, 2007.

[4] N. W. H. Bulten, Numerical Analysis of a Waterjet Propulsion System (Dissertation), Eindhoven, Netherlands: Eindhoven University of Technology, 2006.

[5] C. J. Chesnakas, "Velocity Measurements Inside the Pump of the Gulf Coast Waterjet Tow Tank Model 5600," NSWC-CD, Bethesda, MD, 2003.

[6] L. B. Crook, "Powering Predictions For the R/V Athena (PG 94) Represented by Model 4950-1 with Design Propellers 4710 and 4711," NSWC-CD, Bethesda, MD, 1981.

[7] J. N. Newman. *Marine Hydrodynamics.* MIT Press. Cambridge, MA USA. 1977.

[8] P. Spalart and S. Allmaras, "A one-equation turbulence model fo aerodynamic flows," *La Recherche Aerospatiale, Vol. 1,* pp. 5-21, 1994

[9] ANSYS Inc., "ANSYS FLUENT 13.0 Theory Guide," Ansys Inc, Canonsburg, PA, 2010.

[10] T. Van Terwisga (Chairman), "The Specialist Committee on Validation of Waterjet Test Procedures," in *Proceedings of the 23rd ITTC – Volume II*, Venice, 2002.

[11] T. Van Terwisga (Chairman), "The Specialist Committee on Validation of Waterjet Test Procedures," in *Proceedings of the 24th ITTC - Volume II*, Edingurgh, 2005.